

Non-local electrical detection of spin-momentum-locked surface currents in the 3D topological insulator BiSbTeSe₂

Shaham Jafarpisheh,^{1,2} Frank Volmer,¹ Zhiwei Wang,^{3,4} Bárbara Canto,⁵ Yoichi Ando,³ Christoph Stampfer,^{1,2} and Bernd Beschoten^{1,*}

¹*2nd Institute of Physics and JARA-FIT, RWTH Aachen University, 52074 Aachen, Germany*

²*Peter Grünberg Institute (PGI-9), Forschungszentrum Jülich, 52425 Jülich, Germany*

³*Physics Institute II, University Cologne, 50937 Cologne, Germany*

⁴*Key Laboratory of Advanced Optoelectronic Quantum Architecture and Measurement, School of Physics, Beijing Institute of Technology, Beijing 100081, P. R. China*

⁵*AMO GmbH, Gesellschaft für Angewandte Mikro- und Optoelektronik, 52074 Aachen, Germany*

The spin-polarized surface states in topological insulators offer unique transport characteristics which make them distinguishable from trivial conductors. Due to the topological protection, these states are gapless over the whole surface of the material. Here, we detect the surface states in the topological insulator BiSbTeSe₂ by electrical means using a non-local transport configuration. We unambiguously probe the spin-momentum locking of the topologically protected surface states by spin-sensitive electrical read-out using ferromagnetic Co/Al₂O₃ electrodes. We show that the non-local measurement allows to probe the surface currents flowing along the whole surface, i.e. from the top along the side to the bottom surface and back to the top surface along the opposite side. This is in contrast to local transport configurations where only the surface states of the one face being in contact to the electrodes can be measured. Our results furthermore exclude the contribution of the bulk to the non-local transport at low temperatures. Increasing the temperature, on the other hand, increases the interaction between bulk and surface states, which shortens the non-local current path along the surface and hence leads to a complete disappearance of the non-local signal at around 20 K. All this demonstrates that the non-local signal at low temperatures is solely due to the topologically protected surface states.

The helical surface states of three-dimensional (3D) topological insulators (TIs) are the result of bulk band inversions which occur, e.g., in the presence of strong spin-orbit coupling [1]. Under an electrical bias voltage, the spin-texture of the surface states leads to a spin-polarized current with the polarization being locked perpendicular to the momentum direction [2, 3]. This unique property makes it possible to control the spin-polarization by reversing the current flow direction. As electrical transport in 3D TIs can also depend on bulk states, various strategies have been followed to pinpoint the contribution of surface states within transport measurements. Examples for these efforts include the tuning of the Fermi level in the bulk band gap by electrical gating and detecting a residual conductivity due to surface states, as well as the measurement of quantum oscillations at large magnetic fields Refs. [4–8]. The direct electrical detection of the spin-polarized surface current by using spin-sensitive ferromagnetic electrodes was first proposed by S. Hong et al. [9]. In this potentiometric measurement technique, the detected electrical voltage depends on the relative orientation of the magnetization direction of the sensing ferromagnetic electrode and the direction of the charge carrier's spin-polarization in the surface states. Therefore, reversing either the magnetization direction of the ferromagnetic electrode by an external magnetic field or reversing the flow direction of the current lead to a sign reversal of the detected voltage. This behavior has indeed been seen in several studies and the current and gate voltage dependency was shown to match the

theoretical understanding of the surface states [10–18].

However, one major controversy in interpreting spin-sensitive transport measurements on bismuth-based topological insulators is the possible contribution from bulk transport (black arrows in Figure 1). Despite major developments in achieving a highly insulating bulk [19], it is still difficult to separate effects coming from bulk states which may show similar transport signatures as the ones expected from surface states [20, 21]. This is a crucial issue in local measurements of the surface states in-between source and drain contacts (transport over these surface states is depicted by the blue area in Figure 1(b)). However, the topologically protected surface states are expected to fully enclose the 3D bulk

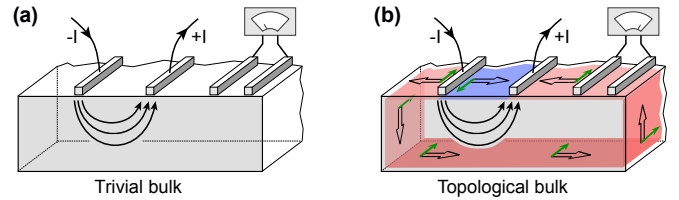


FIG. 1. (a) Distribution of the current inside the bulk of a material with trivial band structure (black arrows). No current is expected under the non-local detection. (b) Distribution of the current inside a 3D topological insulator. The bulk channel (black arrows), the local surface channel directly between source and drain (blue) and a second surface channel (red), which connects source and drain in a non-local manner. The spin polarization directions are shown by green arrows.

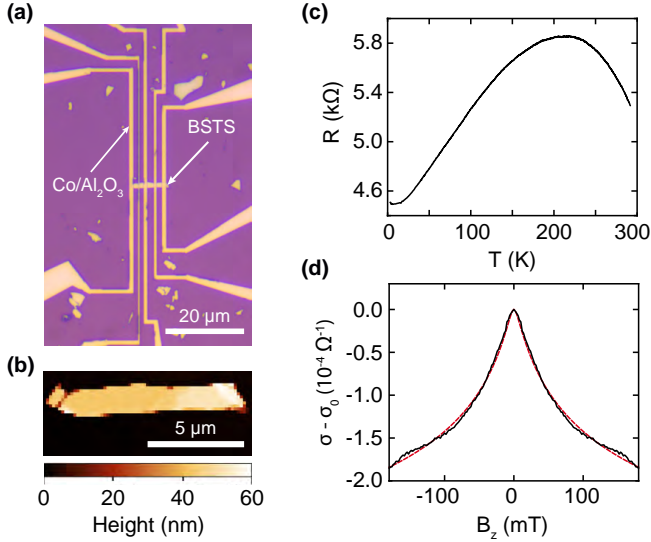


FIG. 2. (a) Optical image of the 40 nm thick exfoliated BSTS flake contacted with Co/Al₂O₃ electrodes. (b) AFM scan of the flake shown in panel (a) before electrode fabrication. (c) Four-probe resistance as a function of temperature. (d) Weak antilocalization measurement at a base temperature of $T = 2$ K. The red dashed line is a fit using the HLN model.

connecting all facets of a strong TI [22]. If surface and bulk states are sufficiently decoupled, a third transport channel opens from source to drain, carrying the current non-locally along the surface even away from the region between source and drain electrodes (see red current path in Figure 1) [23–26]. Because of the spin-momentum locking of the surface states, the electrons contributing to transport in this second surface channel will have an opposite spin orientation compared to the ones of the surface channel which directly connects source and drain electrodes. A non-local [27], spin-sensitive voltage probing of this second surface transport channel thus offers to separate the contributions of surface and bulk states in electrical transport and allows the electrical detection of the spin-momentum-locked surface states.

In this Letter, we report on both local (L) and non-local (NL) electrical probing of the surface states in exfoliated BiSbTeSe₂ (BSTS) flakes [19]. We use Co/Al₂O₃ top electrodes to perform spin-sensitive measurements. In the local configuration the voltage is probed in-between the source and the drain electrodes while in the non-local configuration the voltage outside the source-to-drain region is probed. The local voltages exhibit contributions from both surface and bulk states. However, only in the non-local configuration the voltage probes can solely detect the surface transport through the bottom surface (see red current path in Figure 1(b)). We confirm this surface transport by the correct sign of the non-local voltage and the spin-momentum locking by the reversal of the non-local spin signal when reversing the source-drain current direction. Together with the corresponding measurements in the local configuration,

we confirm spin-momentum locking of the conducting surface states throughout the whole surface layer of the crystal. The spin signals in both detection geometries are strongly temperature dependent and disappear above 50 K which excludes magnetic fringe-fields from the ferromagnetic electrodes as the origin of the spin signals. Furthermore, we identify thermally activated transport through bulk states at higher temperatures which explains the loss of the non-local spin signal due to the disappearance of a decoupled surface state contribution.

The BSTS flakes were prepared by mechanical exfoliation onto SiO₂/Si⁺⁺ substrates. Tunnel-barriers were fabricated by evaporation of an Al seed layer (≈ 1 nm) which got naturally oxidized, followed by thermal atomic layer deposition (ALD) with tri-methylaluminum (TMA) and water as precursors of ≈ 1 nm Al₂O₃. Next, using lithography techniques, patterned cobalt (Co) electrodes were fabricated. An optical image of the device together with an atomic force microscope image of the BSTS-flake after exfoliation are shown in Figures 2(a) and 2(b). The thickness of the flake is ≈ 40 nm. All transport measurements were performed in a continuous-flow cryostat.

The temperature dependent resistance of the device shows a semiconducting behavior at high temperatures and a transition to a metallic regime at $T \approx 200$ K (see Figure 2(c)). This transition corresponds to the depletion of impurity bands within the bulk band gap [6]. The metallic behavior, on the other hand, indicates surface transport which persists down to low temperatures. As it is depicted in Figure 2(d), a low-field magneto-resistance measurement at $T = 2$ K shows the cusp-like feature resulting from weak anti-localization (WAL) [28–32]. The existence of WAL in topological insulators is a hallmark of the strong spin-orbit coupling strength. We use the Hikami-Larkin-Nagaoka (HLN) model [33, 34] for fitting the WAL curve (see red trace in Figure 2(d)) and extract a phase coherence length of around 240 nm. We note that WAL measurements cannot easily distinguish between surface and bulk transport [34].

In order to unambiguously probe the spin momentum locking of the surface states, we now focus on the transport measurements in both local and non-local detection geometries (see Figures 3(a) and 3(b)). By applying a current between the source (S) and drain (D) electrodes in the L configuration, the current may flow through both the top (S_1^L) and bottom (S_2^L) surfaces and through the bulk (B^L) which leads to three parallel conduction channels as it is shown schematically in Figure 3(c). In the L detection configuration, it is therefore not possible to distinguish between surface and bulk contributions since the voltage is measured simultaneously across both.

However, in the NL geometry (Figure 3(b)), conduction through the bottom surface as part of S_2^{NL} can be detected via the voltage probe electrodes 3 and 4. This can be seen in the I-V curves shown in

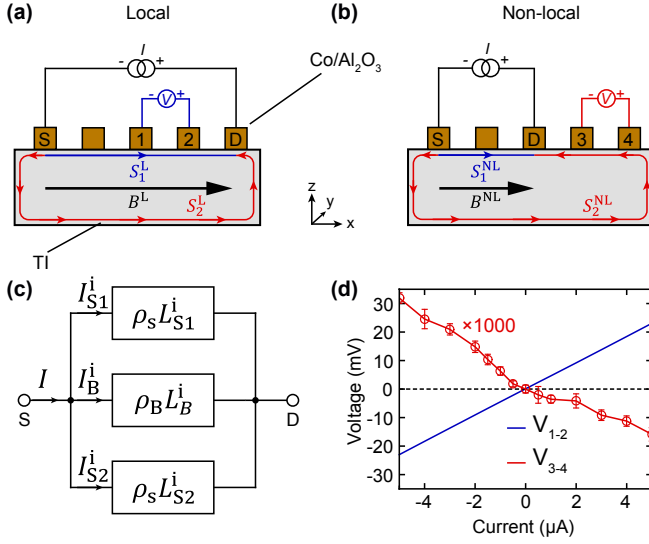


FIG. 3. Schematic illustration of (a) local and (b) non-local measurement configurations. (c) Equivalent circuit of the three contributing transport channels for both configurations. $i = L$ corresponds to the local and $i = NL$ to the non-local detection geometry. $\rho_{B(S)}$ is the normalized resistance per length and $L_{B(S)}^i$ are the lengths of the bulk (surface) channels, which differ between the two measurement configurations (see (a) and (b)). (d) I-V characteristics of the two configurations. The voltage-drop in NL geometry is extracted from the offset voltage in the individual spin-sensitive magnetic measurement traces (see e.g. Figure 5). The amplitude of the NL voltage-drop is magnified by a factor of 1000 for clarity.

Figure 3(d) revealing opposite flow directions of the current in the local and non-local voltages as detected by the sign reversal of the respective voltage drops. In this measurement, the positive sign of current corresponds to electrons moving in the $+x$ direction in the bulk channel. In this case, the voltage drop measured between the local contacts, i.e. $V_L = V_2 - V_1$, has a positive sign (see blue line in Figure 3(d)). Applying a DC current in the same direction in the non-local geometry, however, results in a negative voltage, $V_{NL} = V_4 - V_3$, indicating an electron flow in the $-x$ direction (see red line in Figure 3(d)). This is consistent with the flow directions illustrated in Figures 3(a) and 3(b), respectively, and indicates transport along S_2^{NL} in the non-local configuration. The three orders of magnitude difference in the two measured voltages is an indication that in the local geometry the bulk transport channel is dominant.

The spin-momentum locking of the surface states demands spin-polarization of the non-local current. We therefore use spin sensitive ferromagnetic electrodes to allow for potentiometric detection of the spin-polarized surface current [9]. For this we apply in-plane magnetic fields along the y -direction to reverse the magnetization directions (\vec{M}) of the Co electrodes. As shown in Figure 4, we observe well-defined hysteresis loops in both

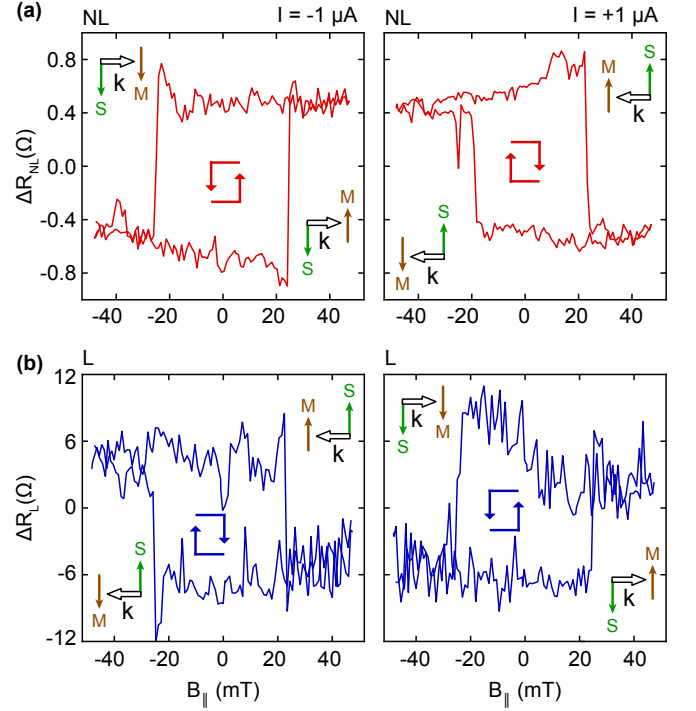


FIG. 4. Potentiometric detection of the spin-polarized current in the topological surface states using (a) non-local and (b) local geometries at $T = 2$ K. Respective electrode configurations are shown in Figures 3(a) and 3(b). The flow direction of electrons (\vec{k}) and their spin-polarization direction (\vec{S}) are shown by black and green arrows, respectively. In-plane magnetization direction of the electrodes (\vec{M}) is indicated using the brown arrows. All measurements show a hysteretic switching of the spin resistance when reversing the magnetization direction of the ferromagnetic detectors by an in-plane external magnetic field B . The sign reversal of the hysteresis curves in the NL configuration (compare left and right panel in (a)) demonstrates the spin-momentum locking of the surface current flowing along the bottom surface of the BiSbTeSe₂ crystal (see S_2^{NL} in 3(b)).

local and non-local configurations which are expected when the contacts are magnetized either parallel or antiparallel to the spin-polarization (\vec{S}) of the surface carriers. We note that the spin sensitive probing of the surface states in TIs has not yet been explored in the NL configuration. Spin diffusion in the bulk channel cannot contribute to the non-local spin signal due to the rapid spin relaxation. The spin diffusion length in BSTS crystal has been estimated to be a few nanometers [35] which is much smaller than the $1.8 \mu m$ minimal distance between the current leads and the non-local detection electrodes. Therefore the non-local switching originates from transport through the surface channel S_2^{NL} only.

It is worth noting that the data shown in Figure 4 are single traces without any additional averaging step. A constant offset value from zero is, however, subtracted considering the sign of the signal as it is explained in the Supporting Information [36]. Due to spin-momentum

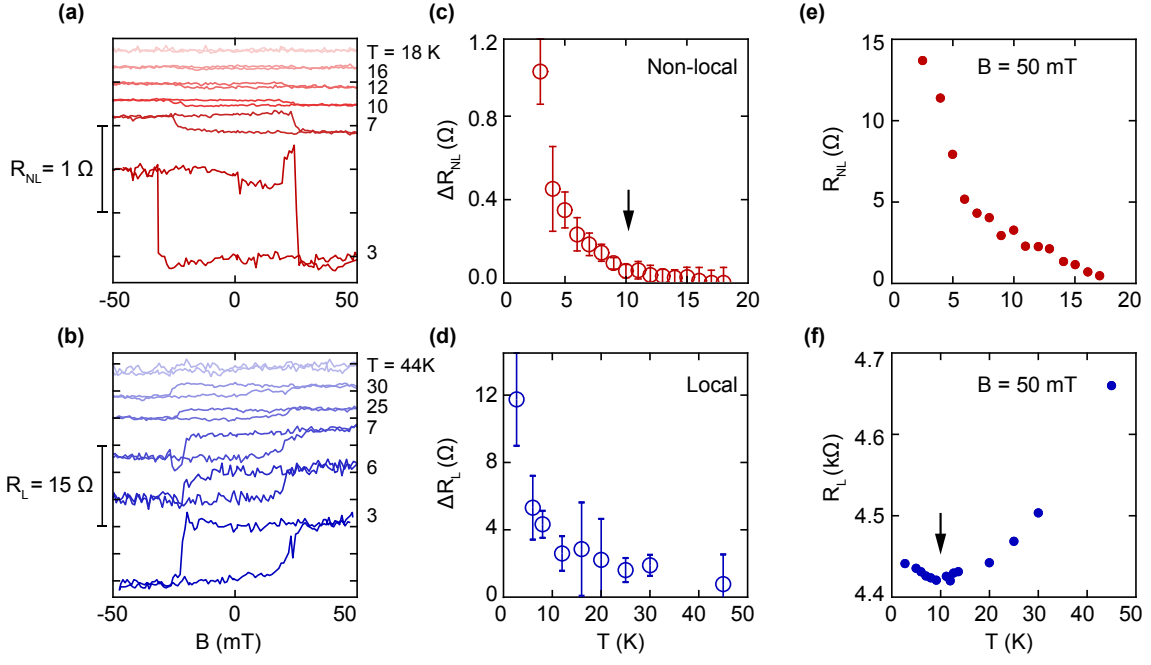


FIG. 5. Evolution of the (a) non-local and (b) local spin signals as a function of temperature. The curves are shifted vertically for clarity. Amplitudes of the spin signals in the (c) non-local and (d) local geometries as a function of temperature. The background offset on which the spin signal is superimposed in (a) and (b) is depicted in (e) for the non-local and in (f) for the local signal by extracting the voltage values at $B = 50$ mT from (a) and (b) and normalized by the applied current between the source and drain electrodes. The black arrows indicate the temperature at which the local voltage in panel (f) shows a minimum and the non-local spin signal in panel (c) disappears.

locking, reversing the electrons' momentum direction (\vec{k}) leads to reversal of the spin-polarization direction of the surface carriers and therefore the reversal of the respective hysteresis curves which is clearly seen in both the L and the NL configurations (compare left and right panels in Figures 4(a) and (b)). Moreover, we observe a reversal of the hysteresis when comparing L and NL curves for the same current direction (compare respective upper and lower panels in Figures 4(a) and (b)). Although the latter sign-reversals are consistent with the reversal of the current flow directions seen in the IV-characteristics discussed above (see Figure 3), we note that several factors other than spin-polarization of surface states can influence the sign of the hysteresis. This includes different relative detection efficiencies of the ferromagnetic detectors considering the absence of a non-magnetic reference electrode in these measurements. The detected spin chemical potential directly depends on the detection efficiency of the ferromagnetic contacts which can be different for each individual electrode. Regardless of the surface spin polarization direction, the sign of the spin signal can be determined by the positioning of the more efficient detector relative to the less efficient one [36]. Furthermore, as Li and co-workers [37] pointed-out, there are other factors such as spin-dependent interface resistances which can affect the sign of the signal. Therefore, we are careful of not making any conclusions about the absolute sign of the

hysteresis curves based on the direction of the current.

We next focus on the amplitude of the spin signals which is given by the difference between the low and high resistance states of the hysteresis curves. In contrast to the three orders of magnitude difference in the offset voltage superimposed to the hysteresis curves (see e.g. I-V characteristics shown in Figure 3(d)), the amplitude of the spin signals differs only by a factor of ~ 10 between the two detection geometries. Interestingly, we can explain this factor very well within a three-channel transport model of the topological insulator. For this, we estimate the currents flowing in the probed surface channels (i.e. the currents responsible for the spin signals), which differ between both configurations due to the different lengths of each channel (see Figures 3(a) and 3(b)). We use a simple equivalent circuit model as shown in Figure 3(c) and apply Ohm's and Kirchhoff's laws. The ratio of the surface to the bulk currents in both L and NL measurement geometries can be written as (see Supporting Information for a more detailed discussion [36]):

$$\frac{I_{S1(2)}^i}{I_B^i} = \frac{\rho_B L_B^i}{\rho_S L_{S1(2)}^i}, \quad i = L, NL, \quad (1)$$

with $I_{S1(2)}^i$ being the current through surface channel 1 (2), I_B^i the current through the bulk, $\rho_{S(B)}$ the normalized resistances for the surface (bulk), and $L_{B,S1(2)}^i$ being

the corresponding length of each individual channel. Using this equation for both local ($i = L$) and non-local ($i = NL$) detection geometries, the ratios of the surface to bulk currents in each case can be extracted. Assuming that the bulk channel is the major conductor of the current between the source and drain electrodes in both geometries ($I_B^L \approx I_B^{NL}$ in our constant current measurements), the ratio between the spin-polarized surface currents responsible for the spin signals in both geometries can be approximated to $I_{S_2}^{NL}/I_{S_1}^L \approx 0.17$. Assuming a similar spin detection efficiency between the electrodes and the well-established fact that the spin-related voltage drop in the hysteresis measurement scales linearly with current [9], we end up with a rather good agreement to the ratio of the spin signal amplitudes $\Delta R_{NL}/\Delta R_L \approx 0.1$ in the two configurations. This supports our notion that both spin signals originate from surface-states. Hence, in the local geometry, the bulk states are only contributing to the offset voltage added to the spin signal (see the I-V characteristic in Figure 3(c)), whereas we solely probe the spin-polarized current of S_2^{NL} in the non-local geometry.

The role of the surface states to the overall transport can further be identified by analyzing the temperature dependent spin signals. Figures 5(a) and 5(b) show the evolution of the hysteresis curves for both local and non-local detection geometries with increasing temperature. The amplitudes of the temperature dependent hysteresis curves, shown in Figures 5(c) and 5(d), are extracted by subtracting the mean value of the low resistive branch from the high resistive branch of the measured data. Furthermore, the magnetic field independent offset values of the hysteresis curves normalized by the value of applied current are extracted at $B = 50$ mT and are plotted in Figures 5(e) for R_{NL} and 5(f) for R_L as a function of temperature. There are two main observations in the temperature dependent measurements. First, the hysteresis in both configurations gets rapidly diminished as the temperature is increased. In fact, the non-local spin signal vanishes around $T \approx 16$ K (Figure 5(c)) while the local spin signal lasts up to $T \approx 45$ K (Figure 5(d)). This demonstrates the spin-related origin of the hysteresis curves since no strong temperature dependency is expected from artifact signals originating from magnetic fringe fields by the electrodes [21]. Second, there is the distinct difference between the evolution of R_L (Figure 5(f)) and the amplitude of local spin signal (ΔR_L) (Figure 5(d)). In the non-local geometry, however, both quantities (ΔR_{NL} and R_{NL}) show a monotonic decrease and disappear completely at a similar temperature (Figures 5(c) and 5(e)). Interestingly, the non-local spin signal in Figure 5(c) becomes very small at a temperature where the local resistance in Figure 5(f) goes through a minimum (see black arrows).

Considering the bulk band gap of BSTS, it is expected that the bulk channel does not contribute to transport at such low temperature. However, it is well known that

in Bi-based 3D TIs it is nearly impossible to achieve a completely insulating bulk [7, 38–43]. The temperature dependent resistance measurement shown in Figure 2(c) reveals a transition from activated to metallic transport below $T \approx 200$ K, which indicates the depletion of bulk states. However, as it was shown previously, variable range hopping (VRH) in the bulk may still contribute to transport at low temperatures [19, 44]. In particular, in BSTS compounds, the compensation of acceptors and donors which can explain the low bulk carrier concentration, results in random local potential fluctuations and therefore the formation of charged puddles. When the size of these puddles gets large enough, charge carriers can tunnel between neighboring puddles and can therefore form a parallel conduction channel which couples to the surface states and gives rise to additional scattering of surface carriers. This mechanism limits the spin-polarized transport on the surface and therefore leads to the suppression of the non-local signal [45]. The temperature dependent VRH transport is predicted to be weaker than a simple thermally activated transport, $R \propto \exp[(T_0/T)^x]$ with $x < 1$ for a 3D system [44]. As shown in the Supporting Information [36], this is in agreement with the temperature dependent local voltage for $T < 20$ K. Increasing the temperature activates the hopping transport in the bulk and limits the transport through the surface states and therefore explains the disappearance of the non-local signals.

In conclusion, we have measured the spin-momentum locking of the surface currents along the whole surface of BiSbTeSe₂ by non-local spin-sensitive voltage probing without contributions from bulk transport. This is in contrast to local measurement configuration where the probing of surface transport is limited to the region in-between source and drain contacts. In this technique, the local voltage-probes typically measure both surface and bulk transport. Previous studies of the spin-momentum locking and the peculiar spin textures of 3D-TIs were limited either to the direct probing of the top surface of the material or to indirect measurements of the spin texture of a buried 3D-TI surface by, for example, proximity coupling to other 2D materials such as graphene [46–49]. Our study demonstrates that the surface currents of a buried TI surface in contact to an insulator (SiO₂ in our case) can be directly measured by non-local transport configurations, which allows to probe spin-momentum locking of buried surfaces in more advanced van der Waals heterostructures.

We gratefully acknowledge helpful discussions with M. Morgenstern. This project has received funding from the European Union’s Horizon 2020 research and innovation programme under grant agreement No 785219 (Graphene Flagship) and No 796388 (ECOMAT), the Virtual Institute for Topological Insulators (Jülich-Aachen-Würzburg-Shanghai), the

Deutsche Forschungsgemeinschaft (DFG, German Research Foundation) under Germany's Excellence Strategy - Cluster of Excellence Matter and Light for Quantum Computing (ML4Q) EXC 2004/1 - 390534769 (Gefördert durch die Deutsche Forschungsgemeinschaft im Rahmen der Exzellenzstrategie des Bundes und der Länder - Exzellenzcluster Materie und Licht für

Quanteninformation (ML4Q) EXC 2004/1 - 390534769), through DFG/SPP 1666 (BE 2441/8-2), and by the Helmholtz Nano Facility [50]. The work at Cologne was furthermore funded by the DFG under project number 277146847 - CRC 1238 (Subprojects A04) - and project number 398945897.

-
- * e-mail: bernd.beschoten@physik.rwth-aachen.de
- ¹ C. L. Kane and E. J. Mele, *Phys. Rev. Lett.* **95**, 226801 (2005).
 - ² M. Z. Hasan and C. L. Kane, *Rev. Mod. Phys.* **82**, 3045 (2010).
 - ³ Y. Ando, *J. Phys. Soc. Jpn.* **82**, 102001 (2013).
 - ⁴ D. Kim, S. Cho, N. P. Butch, P. Syers, K. Kirshenbaum, S. Adam, J. Paglione, and M. S. Fuhrer, *Nat. Phys.* **8**, 459 (2012).
 - ⁵ R. Yoshimi, A. Tsukazaki, Y. Kozuka, J. Falson, K. S. Takahashi, J. G. Checkelsky, N. Nagaosa, M. Kawasaki, and Y. Tokura, *Nat. Commun.* **6**, 6627 (2015).
 - ⁶ Z. Ren, A. A. Taskin, S. Sasaki, K. Segawa, and Y. Ando, *Phys. Rev. B* **82**, 241306 (2010).
 - ⁷ D.-X. Qu, Y. S. Hor, J. Xiong, R. J. Cava, and N. P. Ong, *Science* **329**, 821 (2010).
 - ⁸ J. Xiong, A. C. Petersen, D. Qu, Y. S. Hor, R. J. Cava, and N. P. Ong, *Physica E* **44**, 917 (2012).
 - ⁹ S. Hong, V. Diep, S. Datta, and Y. P. Chen, *Phys. Rev. B* **86**, 085131 (2012).
 - ¹⁰ C. H. Li, O. M. J. van 't Erve, J. T. Robinson, Y. Liu, L. Li, and B. T. Jonker, *Nat. Nanotechnol.* **9**, 218 (2014).
 - ¹¹ K. Vaklinova, K. Polyudov, M. Burghard, and K. Kern, *J. Phys.: Condens. Matter* **30**, 105302 (2018).
 - ¹² A. Dankert, J. Geurs, M. V. Kamalakar, S. Charpentier, and S. P. Dash, *Nano Lett.* **15**, 7976 (2015).
 - ¹³ A. Dankert, P. Bhaskar, D. Khokhriakov, I. H. Rodrigues, B. Karpiak, M. V. Kamalakar, S. Charpentier, I. Garate, and S. P. Dash, *Phys. Rev. B* **97**, 125414 (2018).
 - ¹⁴ J. Tian, I. Miotkowski, S. Hong, and Y. P. Chen, *Sci. Rep.* **5**, 14293 (2015).
 - ¹⁵ J. S. Lee, A. Richardella, D. R. Hickey, K. A. Mkhoyan, and N. Samarth, *Phys. Rev. B* **92**, 155312 (2015).
 - ¹⁶ J. Tang, L.-T. Chang, X. Kou, K. Murata, E. S. Choi, M. Lang, Y. Fan, Y. Jiang, M. Montazeri, W. Jiang, Y. Wang, L. He, and K. L. Wang, *Nano Lett.* **14**, 5423 (2014).
 - ¹⁷ Y. Ando, T. Hamasaki, T. Kurokawa, K. Ichiba, F. Yang, M. Novak, S. Sasaki, K. Segawa, Y. Ando, and M. Shiraishi, *Nano Lett.* **14**, 6226 (2014).
 - ¹⁸ F. Yang, S. Ghatak, A. A. Taskin, K. Segawa, Y. Ando, M. Shiraishi, Y. Kanai, K. Matsumoto, A. Rosch, and Y. Ando, *Phys. Rev. B* **94**, 075304 (2016).
 - ¹⁹ Z. Ren, A. A. Taskin, S. Sasaki, K. Segawa, and Y. Ando, *Phys. Rev. B* **84**, 165311 (2011).
 - ²⁰ A. Yu. Kuntsevich, A. V. Shupletsov, and G. M. Minkov, *Phys. Rev. B* **97**, 195431 (2018).
 - ²¹ E. K. de Vries, A. M. Kamerbeek, N. Koirala, M. Brahlek, M. Salehi, S. Oh, B. J. van Wees, and T. Banerjee, *Phys. Rev. B* **92**, 201102 (2015).
 - ²² L. Fu, C. L. Kane, and E. J. Mele, *Phys. Rev. Lett.* **98**, 106803 (2007).
 - ²³ S. Wolgast, Ç. Kurdak, K. Sun, J. W. Allen, D.-J. Kim, and Z. Fisk, *Phys. Rev. B* **88**, 180405 (2013).
 - ²⁴ D. J. Kim, S. Thomas, T. Grant, J. Botimer, Z. Fisk, and J. Xia, *Sci. Rep.* **3**, 3150 (2013).
 - ²⁵ C. Shekhar, C. E. ViolBarbosa, B. Yan, S. Ouardi, W. Schnelle, G. H. Fecher, and C. Felser, *Phys. Rev. B* **90**, 165140 (2014).
 - ²⁶ J. Lee, J.-H. Lee, J. Park, J. S. Kim, and H.-J. Lee, *Phys. Rev. X* **4**, 011039 (2014).
 - ²⁷ M. Drögeler, C. Franzen, F. Volmer, T. Pohlmann, L. Banszerus, M. Wolter, K. Watanabe, T. Taniguchi, C. Stampfer, and B. Beschoten, *Nano Letters* **16**, 3533 (2016).
 - ²⁸ S.-P. Chiu and J.-J. Lin, *Phys. Rev. B* **87**, 035122 (2013).
 - ²⁹ H.-Z. Lu and S.-Q. Shen, *Phys. Rev. B* **84**, 125138 (2011).
 - ³⁰ H.-Z. Lu, J. Shi, and S.-Q. Shen, *Phys. Rev. Lett.* **107**, 076801 (2011).
 - ³¹ Y. S. Kim, M. Brahlek, N. Bansal, E. Edrey, G. A. Kapilevich, K. Iida, M. Tanimura, Y. Horibe, S.-W. Cheong, and S. Oh, *Phys. Rev. B* **84**, 073109 (2011).
 - ³² D. Kim, P. Syers, N. P. Butch, J. Paglione, and M. S. Fuhrer, *Nat. Commun.* **4**, 2040 (2013).
 - ³³ S. Hikami, A. I. Larkin, and Y. Nagaoka, *ptp.* **63**, 707 (1980).
 - ³⁴ R. Ockelmann, A. Müller, J. H. Hwang, S. Jafarpisheh, M. Drögeler, B. Beschoten, and C. Stampfer, *Phys. Rev. B* **92**, 085417 (2015).
 - ³⁵ Y. Liu, J. Besbas, Y. Wang, P. He, M. Chen, D. Zhu, Y. Wu, J. M. Lee, L. Wang, J. Moon, N. Koirala, S. Oh, and H. Yang, *Nat. Commun.* **9**, 2492 (2018).
 - ³⁶ See Supporting Information [URL will be inserted by publisher] for additional details on the background subtraction from the spin signal, parallel resistor circuit analysis and temperature dependency of bulk conductivity.
 - ³⁷ C. H. Li, O. M. J. van 't Erve, C. Yan, L. Li, and B. T. Jonker, *Sci. Rep.* **9**, 6906 (2019).
 - ³⁸ J. Xiong, Y. Luo, Y. Khoo, S. Jia, R. J. Cava, and N. P. Ong, *Phys. Rev. B* **86**, 045314 (2012).
 - ³⁹ J. G. Checkelsky, Y. S. Hor, M.-H. Liu, D.-X. Qu, R. J. Cava, and N. P. Ong, *Phys. Rev. Lett.* **103**, 246601 (2009).
 - ⁴⁰ N. P. Butch, K. Kirshenbaum, P. Syers, A. B. Sushkov, G. S. Jenkins, H. D. Drew, and J. Paglione, *Phys. Rev. B* **81**, 241301 (2010).
 - ⁴¹ J. G. Analytis, J.-H. Chu, Y. Chen, F. Corredor, R. D. McDonald, Z. X. Shen, and I. R. Fisher, *Phys. Rev. B* **81**, 205407 (2010).
 - ⁴² K. Eto, Z. Ren, A. A. Taskin, K. Segawa, and Y. Ando, *Phys. Rev. B* **81**, 195309 (2010).
 - ⁴³ Z. Ren, A. A. Taskin, S. Sasaki, K. Segawa, and Y. Ando, *Phys. Rev. B* **84**, 075316 (2011).
 - ⁴⁴ B. Skinner, T. Chen, and B. I. Shklovskii, *Phys. Rev. Lett.* **109**, 176801 (2012).

- ⁴⁵ H. Velkov, G. N. Bremm, T. Micklitz, and G. Schwiete, Phys. Rev. B **98**, 165408 (2018).
- ⁴⁶ K. Song, D. Soriano, A. W. Cummings, R. Robles, P. Ordejón, and S. Roche, Nano Lett. **18**, 2033 (2018).
- ⁴⁷ L. Zhang, B.-C. Lin, Y.-F. Wu, H.-C. Wu, T.-W. Huang, C.-R. Chang, X. Ke, M. Kurttepeli, G. V. Tendeloo, J. Xu, D. Yu, and Z.-M. Liao, ACS Nano **11**, 6277 (2017).
- ⁴⁸ S. Jafarpisheh, A. W. Cummings, K. Watanabe, T. Taniguchi, B. Beschoten, and C. Stampfer, Phys. Rev. B **98**, 241402 (2018).
- ⁴⁹ K. Vaklinova, A. Hoyer, M. Burghard, and K. Kern, Nano Lett. **16**, 2595 (2016).
- ⁵⁰ Research Center Jülich GmbH, HNF - Helmholtz Nano Facility, J. Large Scale Res. Facil. (JLSRF) **3**, A112 (2017).
-

Supplemental Material: Non-local electrical detection of spin-momentum-locked surface currents in the 3D topological insulator BiSbTeSe₂

S1. BACKGROUND SUBTRACTION FROM THE SPIN SIGNAL

In the following we show that the correct background subtraction of magnetic-field-independent voltages is crucial to obtain the correct signs of the magnetic hysteresis loops of the respective spin signals. Fig. S1(a) shows a set of raw data of the non-local voltage measured with a DC current applied in two opposite directions. It can be seen that the sign of the background also depends on the current direction. However, the shape of the signal is similar in both cases, i.e. the red trace is above the blue trace. But considering the different sign of the background signal, the similar shapes yield to different trends: Going from negative to positive magnetic fields (blue curves), the signal increases in case of $I = 2 \mu\text{A}$, whereas it decreases in case of $I = -2 \mu\text{A}$. When removing the background (see Figs. S1(b) and S1(c)), its sign should also be considered. From the measurements shown in Fig. S1 it can be concluded that the sign of the spin signal indeed depends on the direction of the current.

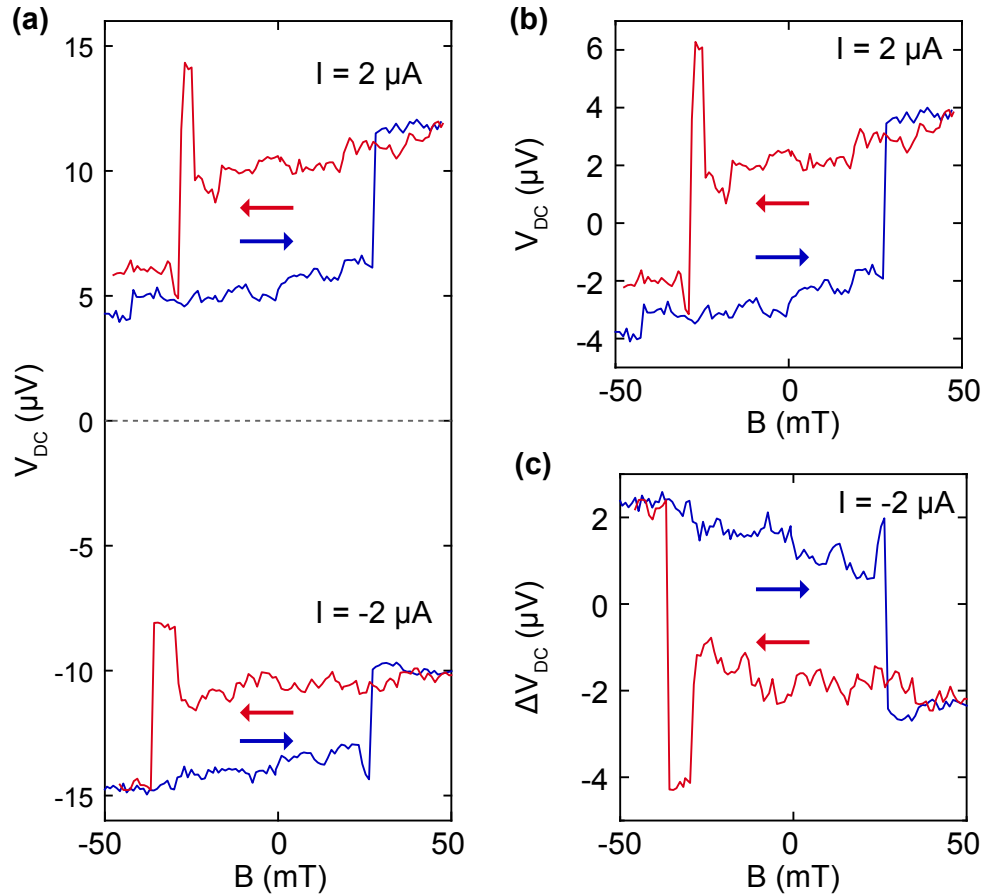


FIG. S1. (a) spin signal with a DC current applied in two opposite directions. The spin signal with (b) $I = 2 \mu\text{A}$ and (c) $I = -2 \mu\text{A}$ after subtracting the magnetic independent offset value and considering the correct sign.

S2. CIRCUIT ANALYSIS OF THE PARALLEL CONDUCTION CHANNELS

Schematic views of the local and non-local detection configurations in addition to the corresponding dimensions are shown in Fig. S2. Parts (c) and (d) depict the equivalent circuits of the local and non-local configurations respectively.

In the local detection geometry (Fig. S2(c)) we can write:

$$\frac{I_{S1}^L}{I_B^L} = \frac{\rho_B L_B^L}{\rho_S L_{S1}^L} \Rightarrow I_{S1}^L = \frac{I_B^L \rho_B L_B^L}{\rho_S L_{S1}^L}, \quad (S1)$$

and similarly in the non-local geometry (Fig. S2(d)):

$$\frac{I_{S2}^{NL}}{I_B^{NL}} = \frac{\rho_B L_B^{NL}}{\rho_S L_{S2}^{NL}} \Rightarrow I_{S2}^{NL} = \frac{I_B^{NL} \rho_B L_B^{NL}}{\rho_S L_{S2}^{NL}}. \quad (S2)$$

The ratio of L and NL surface currents can be extracted using Eq. S1 and Eq. S2 as:

$$\frac{I_{S2}^{NL}}{I_{S1}^L} = \frac{L_{S1}^L}{L_{S2}^{NL}} \frac{L_B^{NL}}{L_B^L} \frac{I_B^{NL}}{I_B^L}. \quad (S3)$$

The first and second terms on the right side of the Eq. S3 can be determined from the dimensions shown in Figs. S2(a) and (b) as $L_{S1}^L/L_{S2}^{NL} = 0.48$ and $L_B^{NL}/L_B^L = 0.36$. With the reasonable assumption that the majority of the current is passing through the bulk channel ($I_B^L \approx I_B^{NL}$), the last term in Eq. S3 is ≈ 1 . This simple calculation results in $I_{S2}^{NL}/I_{S1}^L \approx 0.17$, which is very close to the ratio of the spin signal amplitudes in the two detection geometries, $\Delta R_{NL}/\Delta R_L \approx 0.1$.

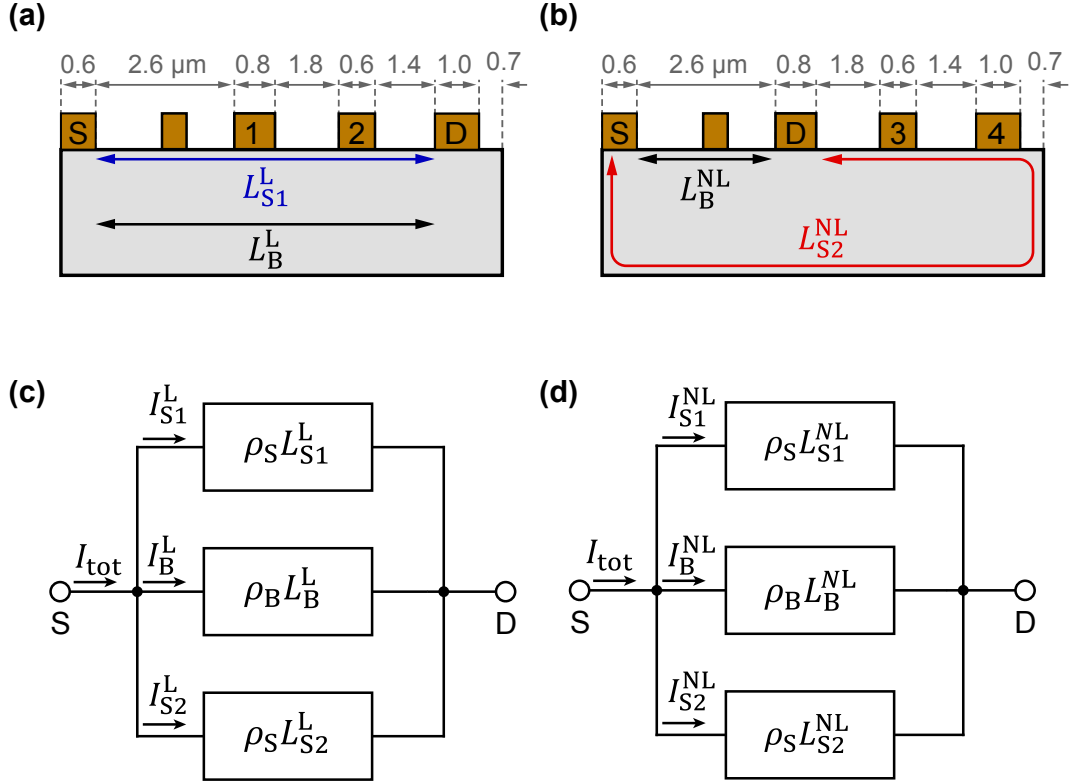


FIG. S2. (a) Local (b) non-local detection geometry and the corresponding dimensions. (c) Equivalent circuit in the local geometry as shown in part (a). (d) Equivalent circuit in the local geometry as shown in part (b).

S3. BULK CONTRIBUTION IN LOW TEMPERATURE TRANSPORT

Fig. S3 depicts the Arrhenius plot showing the increase of the resistance at temperatures below 25 K as it is discussed in the main text. It can be seen that the Arrhenius fit, $R \propto \exp[(T_0/T)^x]$ with $x = 1$ does not represent the measured data. This shows that the temperature dependency is weaker than what is expected from a simple thermally activated transport and points-out toward the VRH mechanism as it is discussed in the main text ($x < 1$).

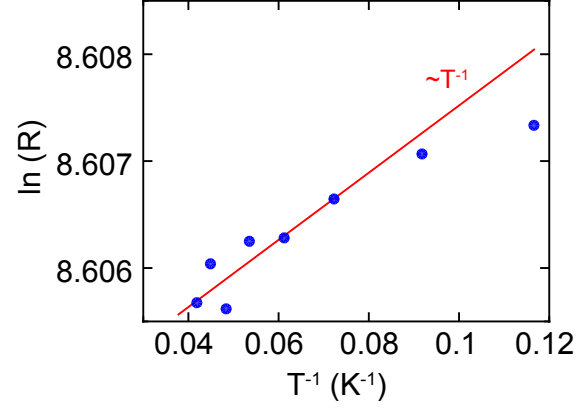


FIG. S3. $\ln(R)$ as a function of $1/T$ at temperatures below 25 K. The red line indicate $\ln(R)$ vs. T^{-1} .